Featured in Physics

Morphological transformation from fibers to sheets in embiopteran silk

Aleimah C. Andrews,[1,2] Sean Duffy,[2,3] Janice S. Edgerly,[1] and Richard P. Barber, Jr.[2,3]
[1]*Department of Biology, Santa Clara University, Santa Clara, California 95053, USA*
[2]*Center for Nanostructures, Santa Clara University, Santa Clara, California 95053, USA*
[3]*Department of Physics, Santa Clara University, Santa Clara, California 95053, USA*

(Received 7 March 2022; accepted 27 May 2022; published 5 July 2022)

Embioptera (webspinners) are insects that construct domiciles using silk produced from their front feet. This silk is the finest known with measured single fiber diameters in the 30–140 nm range. In the wild, some webspinner silk on trees is observed to have a clothlike or shiny sheetlike appearance. Both forms of silk shield the occupants from rain water effectively: presumably valuable in tropical environments. In this article we elucidate the mechanism by which silk fibers are transformed into these structures through interaction with water. We quantify the evaporation rates of single water droplets which have been suspended on unmodified as-spun silk for two Trinidadian arboreal species: *Antipaluria urichi* (Clothodidae) and *Pararhagadochir trinitatis* (Scelembiidae). These rates are compared to those of droplets suspended on rose petals due to similar wetting properties (both hydrophobicity and pinning). We observe that on sufficiently thick silk, droplet evaporation rates decrease with time. This behavior is a result of a thin soluble film developing on the drop surface that later becomes a solid residual film. Experimentally verified theoretical models are invoked to support the results.

DOI: 10.1103/PhysRevE.106.014801

I. INTRODUCTION

Embioptera is an order of insects more commonly known as webspinners; a distinguishing characteristic is that they produce silk from their front tarsi (feet) [Figs. 1(a) and 1(d)]. An estimated 2000 species occur worldwide. Unlike insects which produce 5–10 μm diameter silk as part of their metamorphosing process (e.g., cocoon construction by domesticated silkworms, *Bombyx mori*) or spiders which use silk to catch prey (1–4 μm), webspinners use their silk for constructing domiciles where they gain protection from the elements and natural enemies [1,2]. They produce the finest known natural silks; a recent study of nine species found diameters in the 30–140 nm range [3]. The especially fine diameters of embiopteran silks appears to set them apart from the industrial and applied work conducted thus far that have focused on the macroscale silks of silkworms and spiders [4–7]. The characteristics of the nanoscale embiopteran silks remain largely unexplored despite some progress in characterizing proteins [8], genes [9–12], and ecological contexts of their silk [13,14]; however, many questions remain about the qualities of these natural fibers. Our report seeks to further explore an intriguing characteristic that typifies their silk: the interaction between silk and water [3,14,15].

Webspinner silk domiciles fall into two general categories: in leaf litter or on tree bark (arboreal) [1,16]. Continuing an ongoing comparison, we focus on two arboreal species found in Trinidad, *Antipaluria urichi* (Clothodidae) and *Pararhagadochir trinitatis* (Scelembiidae) [14]. They live in colonies exposed on tree bark and other vertical surfaces that support the growth of epiphytic algae and lichens, upon which they graze. Silk forms a covering that protects them from rain and natural enemies. Field observations have shown that their silk is waterproof but transforms when wetted.

Detailed investigation of the tarsal silk glands has characterized the mechanism of silk extraction. Büsse *et al.* discovered that webspinners produce a silk dope within the silk glands and when the hairlike silk ejectors are pressed against the surface an adhesion disk forms to stick the silk to the substrate [17]. The insects then pull the foot back, shearing the emerging silk dope into solid silk fibers. This process is known commonly as "spinning silk." That they hold their feet in seemingly peculiar orientations suggests that the extraction of silk is involuntary and may account for their proclivity to run backward with their silk ejectors held up off the ground [17]. Microscopic imaging of the tarsi also confirms that the silk is produced in bundles of single fibers with each fiber emerging from one silk gland [8]. This observation contrasts with some cricket species which can produce silk in various morphologies (sheets as well as fibers) [18].

The small diameter range of webspinner silk is inaccessible with standard optical microscopy, so our investigations utilize a Hitachi S-4800 scanning electron microscope (SEM). In order to visualize low electrical conductance silk structures, 20–30 nm Al layers are thermally evaporated onto samples before imaging [for example, Figs. 1(c) and 1(f)]. For unaltered and uncoated diameter measurements, a technique was developed to image as-spun fibers on graphite substrates [3]. The graphite allows for sufficient conduction to produce good quality SEM images as long as the fibers themselves are securely fastened by the webspinners to the substrates. The graphite is also a substrate on which the insects are *willing* to spin silk. Our unpublished preliminary observations revealed that they exhibit an aversion to metallic substrates in addition

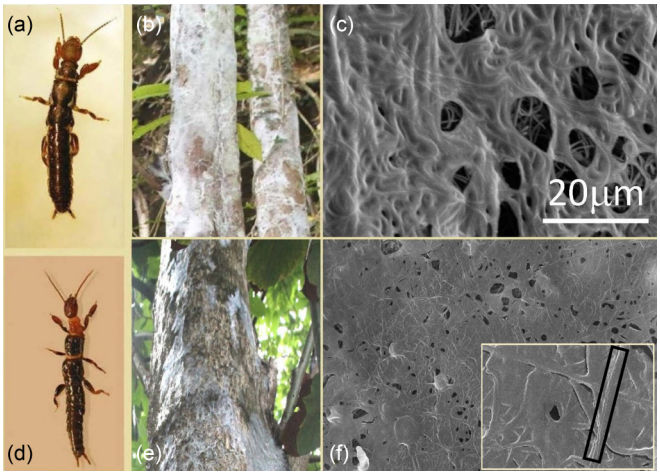

FIG. 1. Comparison images for the two species studied: (a) *Antipaluria urichi* (typical body length, 1.6 cm), (b) previously wetted *A. urichi* silk as it appears on a tree, (c) SEM image of previously wetted *A. urichi* silk, (d) *Pararhagadochir trinitatis* (typical body length, 0.98 cm), (e) previously wetted *P. trinitatis* silk as it appears on a tree, and (f) SEM image of previously wetted *P. trinitatis* silk; inset from the same sample at 5× relative magnification with an underlying fiber highlighted in a black rectangle. Note the large front tarsi (feet) that contain the silk glands. The white scale bar is 20 μm for both SEM images.

FIG. 2. Graphite substrate for *Pararhagadochir trinitatis*. Grooves shown are 3.2 mm wide and 4.8 mm deep. Circular films from dried water droplets are apparent near the center of the image. In order to encourage the silk placement to be higher, later substrates used a shallower (2.4 mm deep) groove with the same width.

to dielectric materials (e.g., glass and plastic). As a result, we have continued the approach of using graphite substrates whenever possible.

Dry silk forms into different structures after being wetted depending on the species. Figure 1(b) shows the clothlike appearance of the silk from *A. urichi*, while Fig. 1(e) displays the shiny plastic-sheet-like appearance of *P. trinitatis* silk. The difference in the optical quality is due to the characteristic length scale of continuous films formed as the dry silk interacts with the water. If the wavelength of light is shorter than the roughness length scale, then the reflected light will be dull [19]. For Al coated films that also exhibited a shiny metallic appearance, the underlying good electrical conductivity suggested roughness length scales smaller than optical wavelengths [3]. This effect is borne out in the microscopic observation of the wetted silk of the two species [14]. The microscopic difference in the film structure is evident in Figs. 1(c) and 1(f). Also apparent in the SEM images are remnants of an underlying silk fiber support structure [see highlighted detail in Fig. 1(f) inset]. The difference between the two species in how the surface film forms after wetting appears to be related to the packing of the fibers; in general *A. urichi* fibers are more diffuse than *P. trinitatis* fibers. The denser the fibers in a patch, the more continuous the film after wetting [14]. However, *P. trinitatis* is sometimes reluctant to produce thick silk, as our results will show below.

Chemical analysis of webspinner silk by Addison *et al.* [8] has revealed a structure with a water-soluble protein core surrounded by a hydrophobic lipid layer. Their conceptual model suggests a protein core consisting of about 70% β-sheet nanocrystallites surrounded by random domains. Analysis of amino acid sequences for the two silk proteins indicates that both are largely hydrophilic along the length of the protein core [12]. The soluble core surrounded by an insoluble sheath is also consistent with SEM imaging of single fibers that were covered with water and then allowed to dry ([3], Fig. 3(a)). That image shows a ruptured tube-shaped structure surrounded by residue apparently from inside, indicating that the inner material is soluble. Experimental evidence of the insoluble sheath–soluble core structure of the silk fibers coupled with the observation of film structures in previously wetted silk raises another question: How does wetting webspinner silk lead to film formation? In previous work we investigated how water droplets wet the silk of different species: specifically, the contact angle of water drops placed on the silk and the tilt angle for which the silk sheds the drops [3]. Earlier work showed that the unwetted fibers grab onto (pin) the water droplets [15]. Both contact angles and tilt angles for previously wetted samples were lower than those on as-spun silk indicating that the previously wetted samples interacted more strongly with water droplets (more wetting) but also shed them more easily (lower tilt angle) [3]. These results are consistent with the expectation that arboreal silk structures show improved protection after being exposed to rainfall. In the wetting and tilt angle studies, it was also noted that water drops dried more slowly than would be expected for pure water.

Absent from this previous work was a detailed investigation of the structural process by which water droplets transform nanoscale silk fibers into the sheet- or clothlike morphology. In this article we elucidate this mechanism.

II. EXPERIMENTAL METHODS

Graphite substrates were machined with grooves (Fig. 2) and enclosed in Petri dishes containing a few adults and late-stage nymphs of either *A. urichi* or *P. trinitatis* and left for up to a week to allow the insects to produce silk. Because of the different sizes of the two species, two different groove sizes were used. For *P. trinitatis* (body length roughly 1 cm) grooves were initially 3.2 mm wide and 4.8 mm deep. In order to keep the silk closer to the top surface of the graphite, a

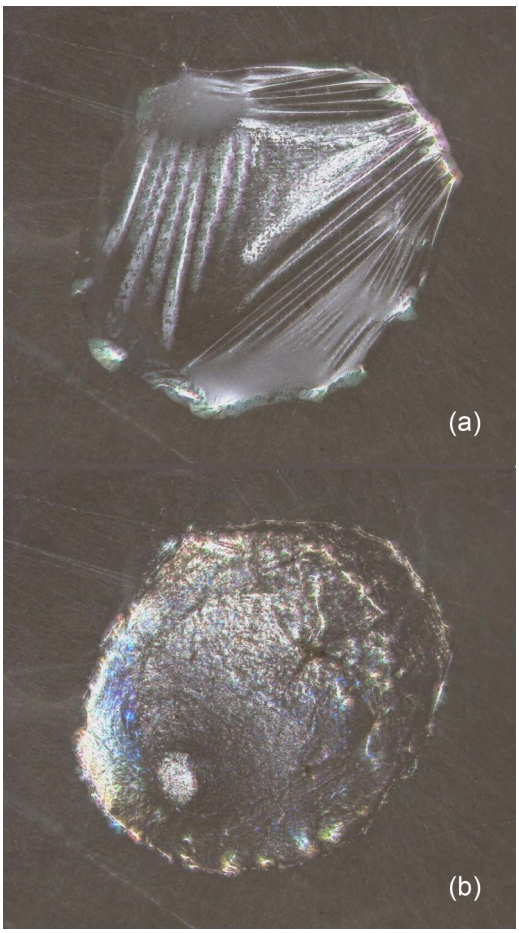

FIG. 3. Asymmetrical 2 μl water drop suspended on *Antipaluria urichi* silk showing (a) wrinkled surface film during drying and (b) final dried film.

later version used grooves that were 2.4 mm deep. *Antipaluria urichi* (body length roughly 1.5 cm) were given larger grooves 6.4 mm wide and 4.8 mm deep due to their larger size and more prolific silk production.

Once the silk was collected, various sized de-ionized water drops were placed onto the regions of silk suspended above the grooves. These water drops were then observed using a Zeta-20 3D (three-dimensional) optical microscope to produce a time series of images as they dried. At the 5× magnification setting on this instrument, we could just fit the largest water drops in our view. At this setting the images had a resolution of 2.7 μm/pixel, so roughly 0.1%–0.2% of the droplet diameters. Two images of a water drop on *A. urichi* silk from such a series are shown in Fig. 3. These are from just before and just after the droplet completely dries. If the droplet in Fig. 3(a) were simply water, we would expect a smooth surface governed by water's surface tension. The apparently wrinkled surface indicates the presence of a film that is determining the texture. Figure 3(b) shows the residual film after the water has completely dried. Note that once the water appeared to be gone, images were taken for several minutes afterward to ensure that no further changes were observed.

This observation (Fig. 3) clarifies the basic mechanism of the film formation. Once water is placed on the silk, it begins to dissolve some of the silk material (presumably the soluble protein core). This material forms a layer on the surface of the water drop and as the water dries the residue is left in the form of a film. This process also explains the inhibited evaporation of the droplet on silk as a film grows to "protect" the top surface from evaporation. Because the silk has two components, the soluble protein core and hydrophobic (insoluble) outer lipid layer, there is a remnant scaffolding on which the dried residual film rests. This structure is apparent in Figs. 1(c) and 1(f). Without the lipid layer, we would expect that water would simply dissolve the fibers leaving voids in the silk layers.

III. RESULTS

In order to quantify the effect of protein films on droplet evaporation, we did side-by-side measurements of droplets on silk and on the nearby graphite (no silk). A typical image series is shown in Fig. 4 at three different times. Figure 4(a) shows both drops less than 1 min ($t = 0$) after they are suspended on the silk (upper left) and placed on the adjacent graphite where no apparent silk is present (lower right). The nominal volume of the drops was 2 μl as indicated by a micropipette. Figure 4(b) shows the situation just as the droplet on the graphite is almost completely dried (mirrorlike appearance due to the flatness of the water). The droplet suspended on the silk is clearly smaller than at $t = 0$. Figure 4(c) shows the residual film on the silk once that droplet has also dried completely. The colors indicate the optical interference effects from the film. The primary data from these measurements were the evaporation time for each drop. A series of these measurements using various volumes is summarized in Fig. 5.

Figure 5 displays the evaporation time of de-ionized water droplets on three substrates: *P. trinitatis* silk, *A. urichi* silk, and graphite. The symbols containing crosses represent results from dual-camera experiments that were performed later (described below). The initial conclusion from Fig. 5 is that water droplets evaporate most quickly from graphite substrates and droplets on silk evaporate at an inhibited rate. However, the total evaporation time data only reveal an *average* evaporation rate. A more useful measurement would be that of droplet volume or surface area as a function of time. In principle, the Zeta-20 microscope should provide 3D images which would allow for volume calculation. However, the water drops themselves also act as an optical component much like a lens. The lens effect on the microscope image software is to interpret the water drop as distorted and inverted (concave instead of convex). To rectify this problem, we added a second microscope (Celestron Model 44301 Mini Handheld Digital Microscope) that allowed for a simultaneous side view of the water droplets. This microscope has the advantage of a small size that allows it to be positioned close to the optical stage of the Zeta-20. Coupled with the Zeta-20 top views, the Celestron has sufficient resolution to derive the droplet volumes (roughly 20 μm/pixel). Example images are shown in Fig. 6.

Given our observation of film formation on droplets suspended on silk, our first conclusion was that the faster evaporation rate from graphite as observed in Fig. 5 was simply due to the lack of this film from the silk.

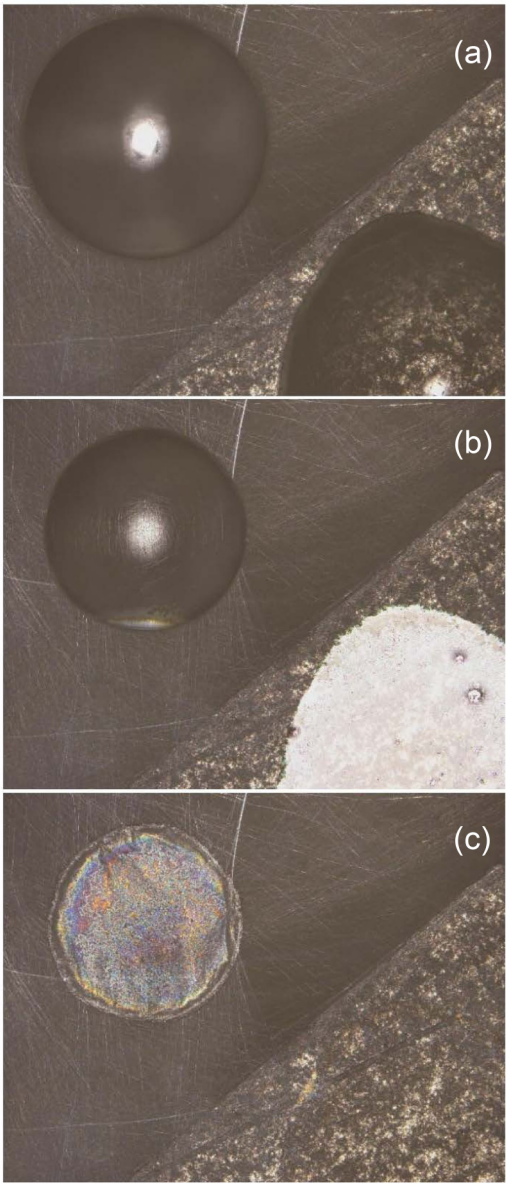

FIG. 4. 2 μl water drops on silk of *Pararhagadochir trinitatis* and graphite: (a) $t = 0$, (b) frame when drop on graphite dries: 28.1 min, and (c) frame when drop on silk dries: 59.8 min.

However, the side-view images in Fig. 6 reveal different droplet shapes, making it clear that a direct comparison of droplets on graphite and silk is problematic. These different shapes lead to very different surface area to volume ratios, a governing factor in evaporation rates (summarized in Fuchs [20]). Previous work has found that the wetting (contact) angle of droplets on *A. urichi* silk is similar to that on rose petals [3,15]. The "rose petal effect" occurs because of the hydrophobic surface along with pinning due to microscopic grooves. Given this more favorable comparison, we changed our control substrate from graphite to rose petals. The side-view images in Fig. 6 make the favorable droplet-shape comparison of the *A. urichi* silk and the rose petal quite apparent.

Length calibration of the side-view images is easily performed using the high precision top-view images and length

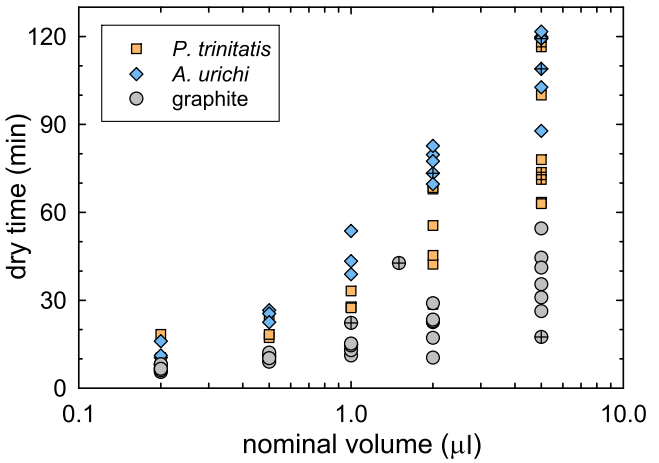

FIG. 5. Graph of total drying time for drops of de-ionized water of various nominal volumes on *Pararhagadochir trinitatis* silk, *Antipaluria urichi* silk, and graphite. The crossed symbols refer to later samples which were also measured with a side-view camera (see Fig. 8).

measurements from the Zeta-20. Figure 7 shows an example of a top view and side view taken at the same time. The six-light illumination from the Celestron camera is apparent in both views: white hexagonal pattern from the side and bluish reflected and refracted spots from the top. These views also confirm the perpendicular line-of-sight direction and allow us to establish the scale (white line as shown). This drop is also displayed in a time-lapse movie available in the Supplemental Material [21]. Once the side-view image is calibrated for length, a perimeter curve that circumscribes the droplet is traced and converted into x-y coordinates using IMAGEJ [22].

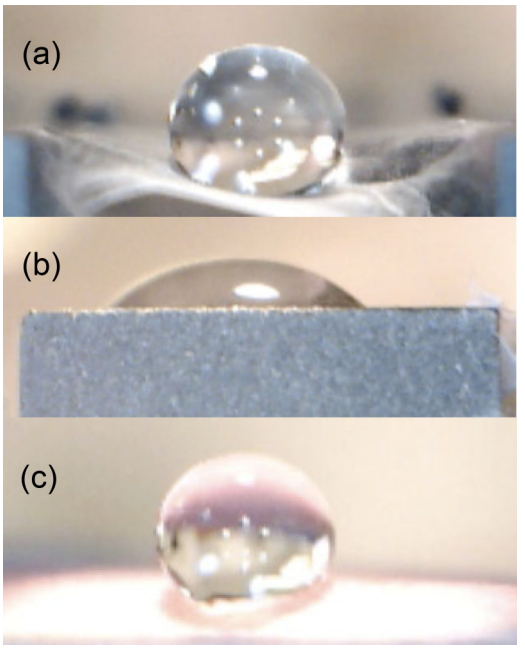

FIG. 6. Side-view images of 2 μl water drops on (a) silk spun by *Antipaluria urichi*, (b) graphite, and (c) a rose petal. The scales are roughly 7 mm across for each image.

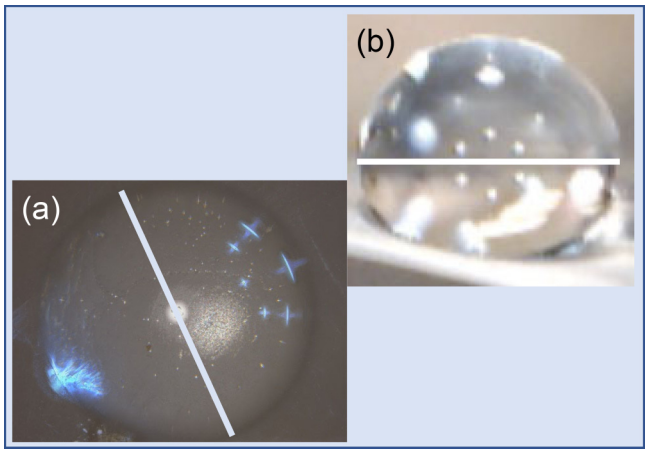

FIG. 7. (a) Top view (Zeta-20) and (b) auxiliary side view (Celestron) of a 9.2 μl water drop suspended on *Antipaluria urichi* silk. The diameter scale bars are 2.76 mm across. The hexagonal array of lights at the center of the side view (from the Celestron camera) correspond to the six blue reflection and refraction points on the upper right of the top view. This alignment indicates the location of the diameter measurements.

Equipped with the length-calibrated drop profile measurements, it is rather straightforward to calculate the drop volume. After horizontally centering the drop, the top and bottom of the drop at the same radial distance from the center are subtracted to produce a height value, h. Note that due to the hydrophobicity of the drops (contact angle greater than 90 °), the bottom surface is often *not* the same as the contact plane of the substrate. Because of left-right asymmetries apparent in some side images, we find the volume for the left and right half of the droplet assuming a half-cylindrical profile for each. The increments of volume $\triangle V$ are therefore given by

$$\triangle V = (\pi r h)\triangle r,$$

where r is the radius of the hemicylindrical shell of thickness $\triangle r$ and height h. Adding up all of the $\triangle V$ values results in the total volume of the droplet. By collecting top and side images over the evaporation time, we produce volume as a function of time $V(t)$ as shown in Fig. 8. Upon first performing this calculation we observed that water droplets that were nominally 5.0 μl according to our micropipette were yielding roughly 7–9 μl in calculated volume. This result suggested an error in our calculation; however, weighing five nominally 5.0 μl drops from the same micropipette on an analytical balance found a mass average 8.4 $\pm$ 0.5 mg (data range 7.9–9.1 mg) confirming that the numerically calculated values are within reason (water density $= 1.0\,\mathrm{mg}/\mu l$). We have since learned that micropipettes require calibration; however, our after-the-fact weighing approach confirms our measured volumes. This calibration issue does affect the abscissa in Fig. 5. We note that this axis *has not* been corrected using this newer information (hence the label "nominal volume"); however, as it is plotted on a logarithmic scale, the general shape and conclusions from those data should not be significantly affected.

It is also possible to use the same profile data to calculate the surface area of the drops. In this case we need to find the incremental area of a semicircular ribbon ΔA, again splitting

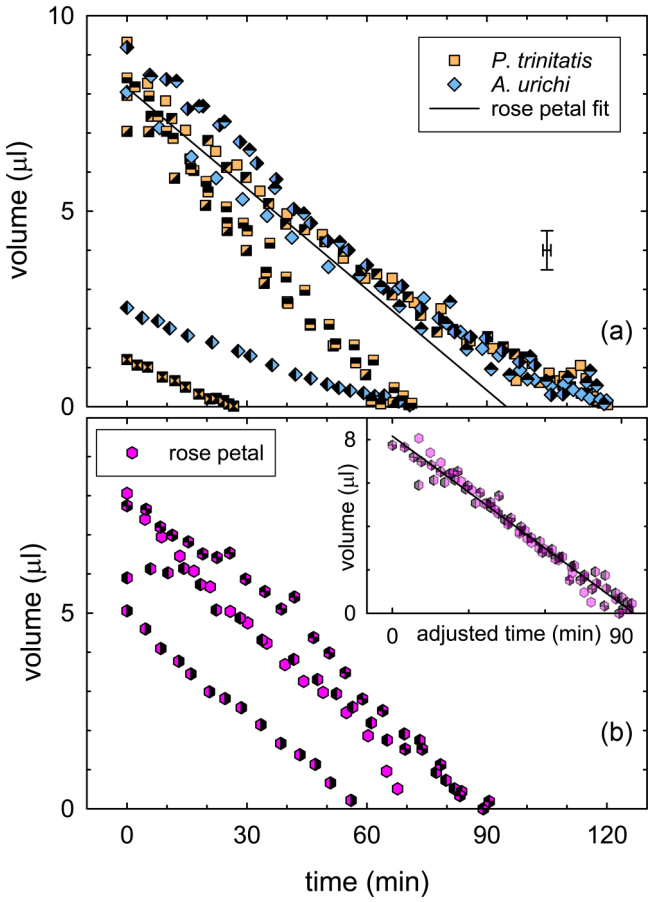

FIG. 8. Droplet volume as a function of time. (a) Results for droplets suspended on *Pararhagadochir trinitatis* silk (squares) and *Antipaluria urichi* silk (diamonds). The solid line is derived from (b) to show the average behavior of droplets on rose petals. Approximate error bars are shown. (b) Results for water on rose petals. The inset to panel b displays the same data but with the times offset so that the 4 μl times coincide. The inset supports the notion that the evaporation rate on rose petals is roughly constant regardless of volume.

the calculation into right and left sides to account for asymmetry. In order to find the area at a given radial distance r, we need a two-dimensional width given by $\Delta w = \sqrt{\Delta x^2 + \Delta y^2}$ so that

$$\Delta A = (\pi r)\Delta w,$$

where x and y are the coordinate locations of points on the circumscribed curve. We have plotted surface area as a function of time $A(t)$ and included that graph in the Supplemental Material as Supplemental Fig. 1 [21]. We will focus on the $V(t)$ data for two primary reasons: $A(t)$ data exhibit more instability as they approach the final value (not zero), and there is ambiguity on how to define the surface area. Since the silk-suspended drops have bottom surfaces that might be at least partially exposed to air, whereas the rose petal drops rest on a textured surface, it is unclear how to correctly compare those two. Also, our pipette "calibration" measurements give us higher confidence in our volume calculations, whereas the area calculations are simply consistent with *reasonable* values.

We have plotted the $V(t)$ data of Fig. 8 in two frames for clarity. Figure 8(a) presents the results for water suspended on silk for the two webspinner species and Figure 8(b) displays the rose petal results. The first observation is that the $V(t)$ data are roughly linear for the rose petals and mostly nonlinear for the silk. Furthermore, the evaporation rates, $\frac{\partial V}{\partial t}$, for the silk samples differ for significantly different starting volumes and typically decrease with time, but the rates for the rose petals look comparable. We note that for droplets starting in the 7–9.5 μl range, there are two branches of data: The upper branch displays three *A. urichi* and two *P. trinitatis* droplets that evaporate in about 2 h, and the lower branch displays three *P. trinitatis* droplets that evaporate in about 1 h.

The similar evaporation rates $\frac{\partial V}{\partial t}$ for the rose petal data motivated us to try collapsing them onto a single curve. Noting that all four curves pass through 4 μl, we linearly extrapolate the time at which 4 μl occurs for each ($T_{4\mu l}$). Subtracting $T_{4\mu l}$ for each of the three leftmost (smaller $T_{4\mu l}$) curves from the rightmost curve (hourglass filled data) yields three time offsets. When these offsets are added to the corresponding time data, we find that all four curves reasonably collapse onto one (inset). For this combined data set, a linear fit looks appropriate and indicates an evaporation rate of 0.086 μl/min.

We have also attempted to determine the typical thicknesses of the residual films. This measurement has proven to be rather challenging as the most relevant samples would be those still suspended on silk. We note that the color fringes evident in Fig. 4(c), suggest thicknesses of the order of optical wavelengths. In order to utilize both the Zeta-20 3D microscope and atomic force microscopy (AFM) to measure either thicknesses or step heights, we added water to silk that is spun directly onto our graphite substrates (i.e., not suspended) and allowed that to dry into films. We have found thickness values ranging from 107 nm to 6 μm for *P. trinitatis* and from 242 nm to 6 μm for *A. urichi*. A summary of these thickness results is presented in Supplemental Fig. 2 in the Supplemental Material [21]. These values are within a reasonable range, but direct comparison with the suspended films might not be justified.

IV. DISCUSSION

A. Experimental results

Most data in Fig. 8(a) indicate that the evaporation *rates* of droplets on silk *decrease* with time. The lowest two curves were started at smaller initial nominal volumes (2.5 μl *A. urichi* and 1.2 μl *P. trinitatis*), so these data do not seem to fit with the larger drop results. Three *P. trinitatis* curves represent drops that dried in about 1 h and do not group well with the upper branch of data (three *A. urichi* samples and two *P. trinitatis* samples taking about 2 h to dry). It was observed that these three faster curves were produced on silk samples that were very sparse. *Pararhagadochir trinitatis* silk was generally found to have denser packing of fibers [14]; however, these three samples reflect *inhibited* or *unwilling* spinning behavior. An indication of this difference is observed in the final dried films for the various experimental runs. The sparse or "thin" silk experiments resulted in very limited residual films whereas the "thick" silk yielded robust, nearly continuous films over the entire region of contact with the droplet. Supplemental Fig. 3 [21] shows images that illustrate this comparison. Furthermore, this definition of thick versus thin correlates exactly with the two *P. trinitatis* evaporation branches.

Focusing on the upper branch of the data (initial volumes in the 8–9.5 μl range and drying times of about 2 h) indicates similar time dependence for both species, and superimposing the fit line from the rose petal data onto the silk droplet data reveals a reasonable agreement with the initial trend. This favorable comparison suggests that the initial evaporation rate of these larger drops is similar to the "common" rate of the drops on the rose petals. Taking the $V(t)$ results for silk-suspended drops along with our model of protein film formation suggests that drops are dissolving and incorporating the protein core as they evaporate. The increasing protein component slows evaporation until the residual film is left behind. Such a trend has been predicted for water droplets with organic surface films: initial evaporation rates similar to that of pure water with slowing rates at later times [23]. It is also notable that as these droplets evaporate, they take on a shape more like the droplets on graphite (see Fig. 6(b) and the evaporation movie in the Supplemental Material [21]). We observe this effect to be due to the pinning of the droplet edges on the silk. The pinning causes the base of the droplet to remain larger than it would be if governed by the surface tension and wetting properties of a new drop [e.g., the shape of Fig. 6(a)]. Given this late-stage shape, we would expect $\frac{\partial V}{\partial t}$ to increase (or at least remain constant) without the presence of any protein film. The *decreasing* $\frac{\partial V}{\partial t}$ further supports our conclusion that the protein film inhibits evaporation. It is also of interest to note that the three "thin" *P. trinitatis* drops evaporate at a faster rate than the rose petal droplets. This result is consistent with sparser silk and a larger effective surface area (bottom and top) from which the drop can evaporate as compared to the rose petals (top only).

B. Theoretical background and model

A comprehensive theoretical treatment of droplet evaporation by Fuchs [20] was rooted in Maxwell's description of diffusion [24] with additional refinement to include heat flow. Previous experimental work [25] had also drawn on diffusion equation solutions [26], and an even earlier derivation [27] was motivated by an experimental study of evaporating iodine spheres [28]. The summarizing prediction of this work is that the evaporation rate of spheres, defined to be mass (or volume) per time, should be proportional to drop radius. An equivalent prediction is that the surface area of a spherical drop should be a linear function of time [20]. Experimental results support either of these relationships [25]. Subsequent experiments considered a more detailed analysis of water droplets evaporating while falling in air of varying humidity [29,30]. For the purposes of our work, the simpler and earlier models appear to be adequate given that we do not control humidity and our drops are stationary. Furthermore, these earlier studies are focused on evaporation from spherical surfaces (iodine spheres, falling water droplets). Although our droplets start out nearly spherical in shape governed by the surface tension of the water combined with the hydrophobicity of the surface (Fig. 6), they eventually become flattened puddles due to

pinning to the surface (see video in the Supplemental Material [21]). We suspect that the linear $V(t)$ behavior of the rose petal droplets is related to their changing shape (aspect ratio).

Fuchs [20] contains a detailed treatment of evaporation rates from different shapes. In particular, he derives an expression for the rate of an oblate ellipse of rotation (flattened ellipsoid). The rate for such an ellipsoid turns out to be

$$I_{\text{ell}} = \frac{4\pi Dc\sqrt{a^2+b^2}}{\cos^{-1}\left(\frac{b}{a}\right)},$$

and the similar version for a sphere,

$$I_{\text{sph}} = 4\pi Dcr,$$

where I is the evaporation rate, a is the semimajor axis, and b is the semiminor axis of the ellipse of rotation, r is the radius of the sphere, D is the diffusion coefficient, and c is the vapor concentration at the surface. The value for D, and also for c, should be the same for both shapes. It is important to note that although our droplets are never full ellipsoids of rotation, their top surfaces can be roughly described as half ellipsoids with the shapes at the earliest times being roughly hemispherical. For comparison we use experimental data digitized from Houghton [25] to calculate and plot volume as a function of time [black curve in Fig. 9(b)]. These data also reflect good agreement with the basic theory because the calculated surface area follows a linear time dependence (not shown here). We now model the same data assuming that the droplets have a fixed semimajor axis (a) equivalent to the initial radius ($a = r$) due to pinning, with the semiminor axis (b, also the thickness of the drop at the center) being reduced while holding the volume constant:

$$\tfrac{4}{3}\pi r^3 = \tfrac{4}{3}\pi a^2 b.$$

At a particular volume, $\frac{4}{3}\pi r^3$, we can then find a value for b, $b = \frac{r^3}{a^2}$.

The ratio, $I_{\text{ell}}/I_{\text{sph}}$, gives us a factor for increased evaporation rates:

$$R = \frac{\sqrt{a^2+b^2}}{a\cos^{-1}\left(\frac{b}{a}\right)}.$$

We now take the differential volume changes from the original spherical data and multiply those by the evaporation rate ratio R to get predicted differential volume changes for ellipsoidal drops. By adding those together we generate a predicted $V(t)$ assuming ellipsoidal drop profiles [Fig. 9(b), red curve]. As would be expected, the new predicted $V(t)$ decreases more quickly as the surface area per volume (hence evaporation rate) is growing faster. Both the evaporation rate ratio R and the predicted $V(t)$ are plotted in Fig. 9. This result supports the conclusion that as the pinned drops evaporate, the evaporation rates increase as their profiles change from almost spherical to very flattened puddles. The predicted red curve is not perfectly linear, but it provides a plausible explanation for the faster and nearly linear $V(t)$ data we observe in our data for rose petals.

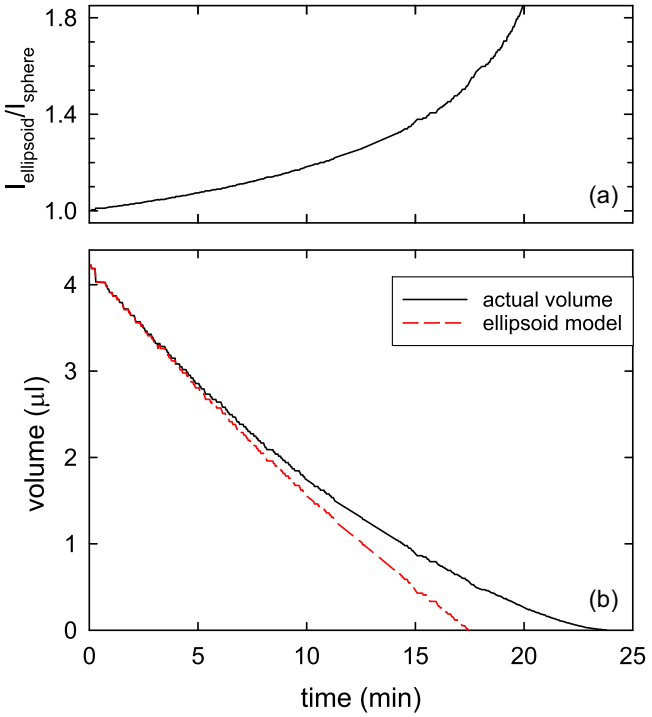

FIG. 9. Modeling of flattening ellipsoid evaporation rates. (a) Calculated ratio of the evaporation rate of an oblate ellipsoid of rotation to that of a sphere (adapted from Fuchs [20]). (b) Data adapted from Houghton [25] of evaporating water droplets (solid black curve). The dashed red curve is our model calculated from assuming the droplets are flattening ellipsoids with a fixed semimajor axis, and the evaporation rate is increased using the factor from (a). Although the red (dashed) line is not exactly linear, the increase in evaporation rate is consistent with our control data for droplets on rose petals.

This modified evaporation model assuming ellipsoidal droplets is consistent with our observations of the roughly linear time dependence of water droplets evaporating from rose petals. Furthermore, a comparison to the rose petal data leads us to conclusions about the similarly shaped droplets on silk. The existence of residual films and the inhibited evaporation from silk on thicker samples as compared to rose petals is consistent with our understanding of the morphological transformation that produces sheet structures. In this case the formation of a protein surface film on the water droplet inhibits evaporation, and it eventually becomes the remnant film. The *faster* drying rate from silk on thinner samples can also be explained by the higher surface area of evaporation compared to the rose petal cases.

V. CONCLUSIONS

We have investigated and described the microscopic process by which embiopteran silk is transformed into sheets or films by water in order to understand its appearance in the wild. These structures help keep the insects dry: an advantage for these tropical species.

We have compared the evaporation of water droplets suspended on both rose petals and embiopteran silk because they share two critical properties: hydrophobicity and pinning. The

similar interactions result in similarly shaped water droplets as they dry. The evaporation rate of the droplets on sufficiently thick silk is inhibited by the presence of a film produced by the soluble protein core. Optical microscope images clearly show a surface film on silk-suspended "water" droplets which presumably consists of this dissolved protein. This film becomes the residual film after drying is complete. The insoluble outer lipid layer provides the support structure as the droplets dry, and SEM images also reveal a structure of these films suspended on the undissolved fibers left behind. This proposed mechanism is supported by a fiber structure with an outer lipid layer and an inner protein core [8]. In addition, our previous SEM observations reveal a distinguishable residue on graphite substrates after wetting single fibers, thereby supporting this water-soluble core model [3]. Droplets on thinner silk evaporated more rapidly than those on rose petals presumably due to their increased evaporation areas (both top and bottom exposed). Although we know that the amino acids in the protein core are hydrophilic [12], the details of the water incursion into the core have not been determined. We have explained the linear time dependence of the evaporation of rose petal drops using a modified ellipsoidal-shape model based on derivations by Fuchs [20] and applied to actual water droplet data [25]. Future plans include improving our measurements of the suspended film thicknesses and characterizing the film material. One possible approach might be to use matrix-assisted laser desorption/ionization time-of-flight (MALDI TOF) mass spectrometry to identify the proteins.

ACKNOWLEDGMENTS

This work was funded by a Santa Clara University Faculty Research Grant. We thank Gary Sloan and Shaun Snyder for technical support.

[1] E. S. Ross, Contributions to the biosystematics of the insect order Embiidina. Part 1. Origin, relationships and integumental anatomy of the insect order embiidina, Occas. Pap. Calif. Acad. Sci. **149**, 1 (2000).

[2] J. S. Edgerly, J. A. Davilla, and N. Schoenfeld, Silk spinning behavior and domicile construction in webspinners, J. Insect Behav. **15**, 219 (2002).

[3] G. Y. Stokes, E. N. DiCicco, T. J. Moore, V. C. Cheng, K. Y. Wheeler, J. Soghigian, R. P. Barber, and J. S. Edgerly, Structural and wetting properties of nature's finest silks (order Embioptera), R. Soc. Open Sci. **5**, 180893 (2018).

[4] H. Tao, D. L. Kaplan, and F. G. Omenetto, Silk materials—a road to sustainable high technology, Adv. Mater. **24**, 2824 (2012).

[5] J. E. Garb, Spider silk: An ancient biomaterial for 21st century research, in *Spider Research in the 21st Century: Trends and Perspectives*, edited by D. Penney (Siri Scientific Press, Manchester, UK, 2013), pp. 252–281.

[6] R. Konwarh, P. Gupta, and B. B. Mandal, Silk-microfluidics for advanced biotechnological applications: A progressive review, Biotechnol. Adv. **34**, 845 (2016).

[7] C. Holland, K. Numata, J. Rnjak-Kovacina, and F. P. Seib, The biomedical use of silk: Past, present, future, Adv. Healthcare Mater. **8**, 1800465 (2019).

[8] J. B. Addison, T. M. Osborn Popp, W. S. Weber, J. S. Edgerly, G. P. Holland, and J. L. Yarger, Structural characterization of nanofiber silk produced by embiopterans (webspinners), RSC Adv. **4**, 41301 (2014).

[9] S. Okada, S. Weisman, H. E. Trueman, S. T. Mudie, V. S. Haritos, and T. D. Sutherland, An Australian webspinner species makes the finest known insect silk fibers, Int. J. Biol. Macromol. **43**, 271 (2008).

[10] M. A. Collin, J. E. Garb, J. S. Edgerly, and C. Y. Hayashi, Characterization of silk spun by the embiopteran, *Antipaluria Urichi*, Insect Biochem. Mol. Biol. **39**, 75 (2009).

[11] M. A. Collin, J. S. Edgerly, and C. Y. Hayashi, Comparison of fibroin cDNAs from webspinning insects: Insight into silk formation and function, Zoology **114**, 239 (2011).

[12] J. R. Harper, N. Sripada, P. Kher, J. B. Whittall, and J. S. Edgerly, Interpreting nature's finest insect silks (order Embioptera): Hydropathy, interrupted repetitive motifs, and fiber-to-film transformation for two neotropical species, Zoology **146**, 125923 (2021).

[13] J. S. Edgerly, Is group living an antipredator defense in a facultatively communal webspinner (Embiidina: Clothodidae)? J. Insect Behav. **7**, 135 (1994).

[14] S. Shenoy, K. Ing, R. P. Barber, E. C. Rooks, and J. S. Edgerly, A multiscale characterization of two tropical embiopteran species: Nano- and microscale features of silk, silk-spinning behavior, and environmental correlates of their distributions, Environ. Entomol. **49**, 1242 (2020).

[15] T. M. Osborn Popp, J. B. Addison, J. S. Jordan, V. G. Damle, K. Rykaczewski, S. L. Y. Chang, G. Y. Stokes, J. S. Edgerly, and J. L. Yarger, Surface and wetting properties of embiopteran (webspinner) nanofiber silk, Langmuir **32**, 4681 (2016).

[16] J. S. Edgerly, Biodiversity of embiodea, in *Insect Biodiversity* (John Wiley & Sons, Ltd, New York, 2018), pp. 219–244.

[17] S. Büsse, T. H. Büscher, E. T. Kelly, L. Heepe, J. S. Edgerly, and S. N. Gorb, Pressure-induced silk spinning mechanism in webspinners (Insecta: Embioptera), Soft Matter **15**, 9742 (2019).

[18] A. A. Walker, S. Weisman, J. S. Church, D. J. Merritt, S. T. Mudie, and T. D. Sutherland, Silk from crickets: A new twist on spinning, PLoS One **7**, e30408 (2012).

[19] L. Gunther, *The Physics of Music and Color* (Springer Science & Business Media, Berlin, 2011).

[20] N. A. Fuchs, *Evaporation and Droplet Growth in Gaseous Media*, 1st ed. (Pergamon, New York, 1959).

[21] See Supplemental Material at http://link.aps.org/supplemental/10.1103/PhysRevE.106.014801 for time-lapse movie of droplet drying, time dependence of droplet surface areas (Supplemental Fig. 1), film thickness measurements (Supplemental Fig. 2), and thick and thin film images (Supplemental Fig. 3).

[22] C. A. Schneider, W. S. Rasband, and K. W. Eliceiri, NIH image to IMAGEJ: 25 years of image analysis, Nat. Methods **9**, 671 (2012).

[23] J. F. Davies, R. E. H. Miles, A. E. Haddrell, and J. P. Reid, Influence of organic films on the evaporation and condensation

of water in aerosol, Proc. Natl. Acad. Sci. USA **110**, 8807 (2013).

[24] J. C. Maxwell, Diffusion, in *The Scientific Papers of James Clerk Maxwell*, edited by W. D. Niven (Cambridge University Press, Cambridge, 2011), pp. 625–646.

[25] H. G. Houghton, A study of the evaporation of small water drops, Physics **4**, 419 (1933).

[26] H. Jeffreys, XXX. Some problems of evaporation, London, Edinburgh Dublin Philos. Mag. J. Sci. **35**, 270 (1918).

[27] I. Langmuir, The evaporation of small spheres, Phys. Rev. **12**, 368 (1918).

[28] H. W. Morse, On evaporation from the surface of a solid sphere. Preliminary note, Proc. Am. Acad. Arts Sci. **45**, 363 (1910).

[29] H. Duguid, A study of the evaporation rates of small freely falling water droplets, Master's thesis, University of Missouri–Rolla, Missouri, 1969.

[30] H. A. Duguid and J. F. Stampfer, The evaporation rates of small, freely falling water drops, J. Atmos. Sci. **28**, 1233 (1971).